THE EUROPEAN PHYSICAL JOURNAL D

Regular Article

Multispectral X-ray imaging with a multichannel Kirkpatrick-Baez microscope for imploded core temperature observation

Wei Wang[1,a], Zhi-Heng Fang[1], Guo Jia[1], Sheng-Zhen Yi[2], Yu-Chun Tu[2], Jing-Tao Zhu[2], Bao-Zhong Mu[2], Hong-Hai An[1], Rui-Rong Wang[1], Zhi-Yong Xie[1], Jun-Jian Ye[1], Xiang-Fu Meng[1], Hua-Zhen Zhou[1], Chen Wang[1], An-Le Lei[1], Zhan-Shan Wang[2], and Si-Zu Fu[1]

[1] Shanghai Institute of Laser Plasma, 1129 Chenjiashan Road, Shanghai 201899, P.R. China
[2] Key Laboratory of Advanced Micro-structured Materials, Tongji University, Shanghai 200092, P.R. China

Abstract. The coupling efficiency of short-pulse ignition laser energy to hot-spot internal energy directly affects the feasibility of fast ignition. Experimental characterization of the hot spot has attracted much attention. Among temperature, density and neutron yield of fast ignition experiments, the temperature of the hot spot has few available diagnostic methods. Multispectral X-ray imaging of hot-spot continuum emission is expected to give the time evolution of the electron temperature distribution. This article describes electron temperature determination from multispectral imaging, a dual-channel X-ray Kirkpatrick-Baez (KB) microscope designed for two-spectral imaging, and the experimental results of hot-core multispectral imaging of an imploded cone-shell target at the SG-II laser facility.

1 Introduction

The heating efficiency of short-pulse ignition laser directly affects the feasibility of fast ignition [1–3]. However, fast-ignition integrated experiments show that the coupling efficiencies of ignition laser energy to hot spot internal energy are quite different from each other [4–7]. Therefore, the hot spot characteristics are still key issues for fast ignition.

The distributions of temperature and density can be used to describe the state of the hot spot. Neutron yield is also an important parameter reflecting the overall heating. Among these physical quantities, the neutron yield has comparatively mature diagnosis method [8], the density can be diagnosed by X-ray [9] or proton [10] radiography, while the hot-spot temperature has few available diagnostic methods. In the case of neutron yield higher than 10^9, the ion temperature can be obtained by measuring neutron spectrum broadening caused by Doppler effects using a time-of-flight neutron spectrometer [8]. However, under low neutron yield experimental conditions, neutron energy spectrum diagnosis relies on costly large detector arrays [11]. In these cases, spatially and temporally resolved temperature measurements are difficult to make.

The hot-spot temperature ranges of interest are sub-keV to several keV. In this case the fuel in the hot spot is fully ionized. X-ray radiation from the hot spot is mainly continuum emission comprising Bremsstrahlung and recombination radiation. Multispectral X-ray imaging of hot-spot continuum emission is expected to give a time evolution of the electron temperature distribution [12].

This method avoids the use of dopants in the target [13], but requires a high-collection-efficiency imaging system. Therefore, multispectral X-ray imaging based on Kirkpatrick-Baez (KB) microscopy [14–16] was developed, which has a higher collection efficiency and higher spatial resolution than a pinhole camera [17], and more controllable working photon energies and spectral resolution [18] than bent crystals imagers [19,20].

This paper presents the derivation of the electron temperature from multispectral imaging, the method of multispectral X-ray KB imaging, and experimental results of hot-core multispectral imaging of imploded cone-shell targets at the SG-II laser facility [3].

2 Electron temperatures derived from continuum emission

X-ray radiation includes spectral line emission from bound-bound transitions, recombination radiation from free-bound transitions and Bremsstrahlung radiation from free-free transitions. When the photon energy $h\nu$ (in units of eV) is greater than $Z^2 R_y$ (where Z is the nuclear charge number and $R_y = 13.6$ eV is the Rydberg energy), X-ray emission is a continuum spectrum composed of Bremsstrahlung radiation and recombination radiation. The Bremsstrahlung radiation power per unit volume, per unit time, per unit photon energy is given by [21,22]:

$$\varepsilon\left(h\nu\right) = \frac{2^5 \pi e^6}{3mc^3}\left(\frac{2\pi}{3km}\right)^{1/2}\frac{Z^2 N_e N_i}{\sqrt{kT}}\exp\left(-\frac{h\nu}{kT}\right)\bar{g}_{ff},$$

(1)

a e-mail: wei_wang@fudan.edu.cn

Table 1. Temperature deviation caused by neglecting external fuel absorption and recombination radiation (RR).

T_{set} (keV)	T_{fit} (keV) 50 mg/cm^2	T_{fit} (keV) 100 mg/cm^2	T_{fit} (keV) 0 mg/cm^2, RR	T_{fit} (keV) 50 mg/cm^2, RR	T_{fit} (keV) 100 mg/cm^2, RR
0.5	0.505	0.521	0.538	0.543	0.562
1.5	1.547	1.707	1.733	1.796	2.015
2.5	2.633	3.132	2.926	3.109	3.830

where N_e and N_i are the number densities of electrons and ions, kT is the plasma temperature in units of eV, and $\bar{g}_{ff}$ is the velocity-averaged free-free Gaunt factor. $\bar{g}_{ff} = \sqrt{\frac{3kT}{\pi h\nu}}$ when $h\nu > kT$ and $h\nu > Z^2 R_y$ [21], and so,

$$\varepsilon\left(h\nu\right) = C \frac{Z^2 N_e N_i}{\sqrt{h\nu}} \exp\left(-\frac{h\nu}{kT}\right), \qquad (2)$$

where $C = \frac{2^5 \pi e^6}{3mc^3}\left(\frac{2}{km}\right)^{1/2}$ is a dimensional constant. If we measure the radiation intensities at two photon energies $h\nu_1$ and $h\nu_2$ ($h\nu_2 > h\nu_1$), dividing $\varepsilon(h\nu_2)$ by $\varepsilon(h\nu_1)$, the result is the temperature,

$$kT = \frac{\Delta h\nu}{\ln\left(\frac{\varepsilon(h\nu_1)\sqrt{h\nu_1}}{\varepsilon(h\nu_2)\sqrt{h\nu_2}}\right)}. \qquad (3)$$

If one substitutes equation (3) back into equation (2), and takes into account $N_e = ZN_i$, the result is an expression for the electron density N_e. Equation (3) shows that only the relative intensities at two photon energies are needed to determine the temperature. An absolute X-ray intensity measurement would be required to measure the density at the same time.

Equation (2) can be rewritten as:

$$\ln\left(\varepsilon\left(h\nu\right)\sqrt{h\nu}\right) = \ln\left(CZ^2 N_e N_i\right) - \frac{h\nu}{kT}, \qquad (4)$$

which is a line. Using relative intensity $\varepsilon(h\nu)$, the slope and then the temperature T can be determined.

By replacing $\bar{g}_{ff}$ in equation (1) with $\frac{Z^2 R_y}{kT}\frac{2}{n^3}G_n \exp(\frac{Z^2 R_y}{n^2 kT})$, one gets the recombination radiation power per unit volume, per unit time, per unit photon energy. The Gaunt factors G_n are within 20% of 1 for $h\nu < 10Z^2 R_y$ [22]. It should be noted that the equation holds only when $h\nu \geqslant Z^2 R_y/n^2$, and otherwise $\varepsilon = 0$.

The measured radiation spectrum of a hot spot is a continuum spectrum comprising both Bremsstrahlung and recombination radiation. Additionally, the absorption of external fuel is different for different photon energies. These factors are not accounted for in the temperature derivation described above. To study the effects of absorption and recombination radiation on temperature measurements, the radiation intensity at photon energies from $2.5-4.5$ keV are calculated for a deuterated-plastic (CD) plasma where $kT = 0.5$ keV, 1.5 keV, and 2.5 keV, as absorbed by CD plasmas with $\rho R = 0$, 50 mg/cm^2, and 100 mg/cm^2, where $kT = 100$ eV. This calculation was done both with and without recombination radiation. Electron temperatures were determined using equation (3). Results in Table 1 show that ignoring absorption and recombination radiation will result in higher measured temperatures. The higher the hot-core temperature or the external fuel density, the greater the deviation of the measured temperature from the actual temperature. That deviation is related to the measured photon energies. For a plasma with given temperature, a reasonable selection of measured photon energies will improve the accuracy of temperature measurement. Of course, experimental measurement errors should also be considered when selecting the measured photon energies.

It can be seen from Table 1 that ignoring recombination radiation affects temperature measurement accuracy more severely. Directly comparing the calculated spectrum including both Bremsstrahlung and recombination radiation with multispectral experimental data will give a more accurate electron temperature. The calculated spectrum can be further corrected if the external fuel areal density is available.

This method of temperature measurement using diagnosis of continuum radiation spectrum is suitable for a medium-temperature hot core with small external fuel density. When the hot-spot temperature is higher than 2.5 keV or the external fuel areal density is higher than 100 mg/cm^2, the temperature measurement error of this method becomes significant (note that the error relates to the measured photon energies). However, in this case the number of nuclear reaction products will be high enough that nuclear diagnosis methods such as neutron spectroscopy can work well.

3 Multispectral imaging using multichannel KB microscope

The imaging system uses KB imaging method [14–16], which uses two orthogonal grazing incident spherical mirrors to produce a two-dimensional image. Compared with pinhole imaging, KB imaging increases photon collection efficiency by an order of magnitude while remaining the same or a little higher spatial resolution (better than 10 μm). Quasi-monochromatic imaging is achieved using multi-layers coated on the mirror to select photons at the reflectance peak, while using an appropriate filter to cut off the low energy portion of the reflection. Multispectral imaging can be achieved with an assembly of multiple mirrors. As shown in Figure 1, to simplify the assembly the same total reflection mirror M_{TR} is shared in one direction for all channels. The M_{TR} was coated with W/B4C
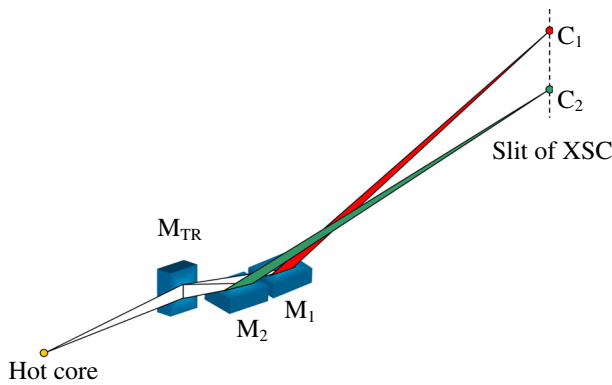
Fig. 1. Schematic of the dual-spectral KB microscope. A total reflection mirror M_{TR} is shared in one direction for all channels. In the other direction each channel uses an independent multilayer mirror to select the imaged photon energy.

Fig. 2. Schematic of the "IN" type object, which was made of Mo with an outer diameter of 2.5 mm and line width of characters "IN" of 30 μm. The dashed line shows the relative position of the streak camera entrance slit. The up-down position of the slit can be determined by line spaces recorded by the camera.

bilayers, X-ray at 8 keV or lower than 5 keV can be reflected. In the other direction each channel uses an independent multilayer mirror to select the imaged photon energy range. Multilayers include top Cr/C bilayers and bottom W/B4C bilayers working at 2.5 keV or 3 keV and 8 keV, respectively. This design makes the system highly extensible, as channels can be easily added by increasing the number of mirrors. This imaging system is also easy to couple with temporal-resolution recording equipment such as a streak camera or a framing camera. The disadvantage is that different channels can have different imaging magnifications, but it is easy to be corrected by image post-processing, and will have no effect on the application of the system.

The multispectral imaging system was assembled using an 8 keV X-ray source open to the atmosphere. A small golden ball (outer diameter of 0.2 mm) and a charge-coupled device (CCD) were used as fiducial markers to indicate the object position and the image position, respectively. At the laboratory site the ball was moved to the target chamber fiducial point (object point) by translating the entire imaging system including the ball and the CCD, then the recording equipment was moved to the image point indicated by the CCD, and then the fiducial ball and CCD were removed. An "IN" type object shown in Figure 2 was used to confirm the position of the streak camera entrance slit. The object was made of Mo with an outer diameter of 2.5 mm and line width of characters "IN" of 30 μm. The dashed line in Figure 2 shows the relative position of the streak camera entrance slit. The up-down position of the slit can be determined by line spaces recorded by the camera.

One-hundred-μm-thick beryllium and 2-μm-thick titanium films were used as filter to cut off the low-energy total reflection photons of the grazing incident mirrors and to shield stray light. The total channel theoretical relative efficiencies of the system, including filter transmittance, mirror reflectance and photocathode spectral response of the streak camera (Axis Photonique: AXIS-PX, CsI photocathode), are shown in Figure 3. The working photon energies of the channels were 2.5 keV and
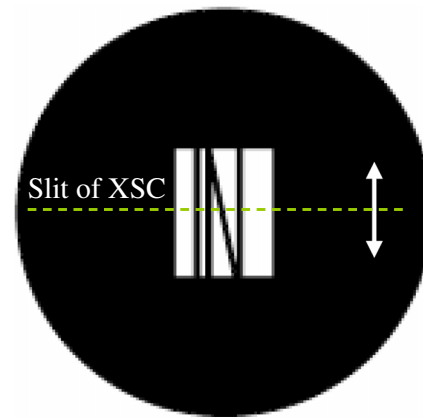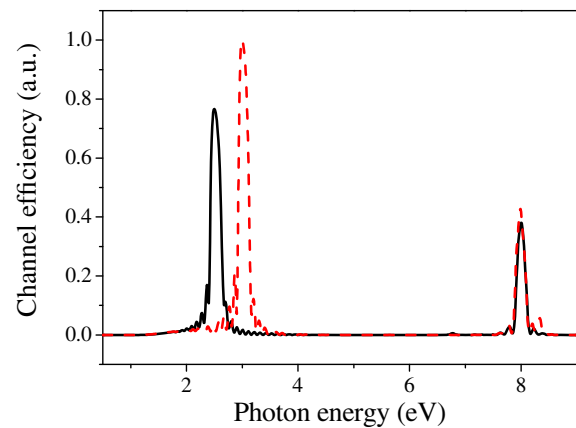

Fig. 3. Channel theoretical relative efficiencies of dual-spectral KB microscope, including filter transmittance, mirror reflectance and photocathode spectral response of the streak camera. The working photon energies are 2.5 keV and 3 keV. 8-keV channels are for assembly.

3 keV, respectively. 8 keV channels were used for assembly. Channel bandwidth was optimized through multi-layer film design to balance the integral reflection efficiency and spectrum resolution.

The contributions of the 8 keV channel increases gradually with kT. Calculation suggests that, for $kT < 2.5$ keV, the radiation intensity at 8 keV is much lower than that at 2.5 keV or 3 keV, and the effect of the 8-keV channel is negligible. When $kT > 2.5$ keV, the contribution of the 8-keV channel should not be ignored. In principle, this problem can be solved. The contribution of the 8-keV channel on intensity can be taken into account by integrating over energy spectrum [17]. Alternatively, an X-ray source with other energy instead of 8 keV, for example, in grazing incident total reflection channel, can be used to assemble the imaging system.
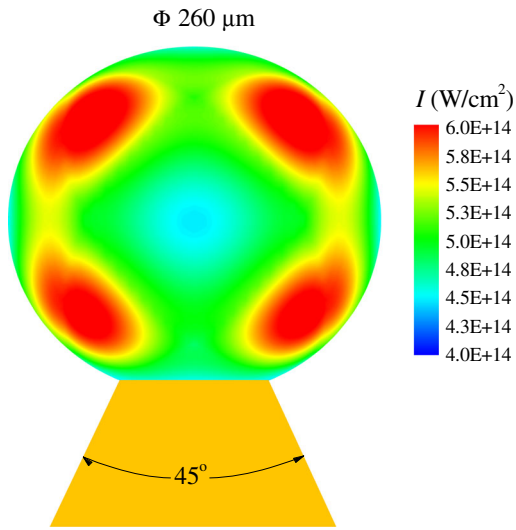
Fig. 4. Schematic of the cone-shell target with laser beam spots on the shell surface. The shell was made of CD with an outer diameter of $\Phi = 260$ μm and a wall thickness of 12 μm. The cone was made of Au with an opening angle of 45° and a wall thickness of 10 μm. Eight laser beams (frequency tripled to 351 nm, defocused to $\Phi = 220$ μm) directly illuminated the shell surface.

4 Experimental results

Experiments were carried out at the SG-II laser facility [3]. The shell of cone-shell target was made of CD with an outer diameter of $\Phi = 260$ μm and a wall thickness of 12 μm. The cone was made of Au with an opening angle of 45° and a wall thickness of 10 μm. Eight laser beams (frequency tripled to 351 nm, 260 J/beam, slightly defocused to $\Phi = 220$ μm) directly illuminated the shell surface. A cone-shell target schematic figure with laser beam spots on the shell surface is shown in Figure 4.

A hot core was produced by shell implosion, which gives a temperature source similar to those found in the hot spots of fast ignition experiments. The hot-core self-emission images at 2.5 keV and 3 keV were recorded by the multispectral X-ray imaging system and the X-ray streak camera. A typical result is shown in Figure 5. The inset at the top-right corner illustrates the orientation of the cone-shell target, and the dashed line shows the relative position of the streak camera entrance slit. The target surface starts radiating at time $t = 0$. The strong light from the imploded hot core can be seen clearly in the image.

The radiation intensity ratio of the two channels was obtained by correcting the line strength shown in Figure 5 using the efficiency shown in Figure 3. Ignoring the recombination radiation and the absorption of outer fuel, the hot-core temperature was obtained using equation (3). The temperature range makes this a reasonable simplification, as discussed in Section 2. The evolution of the core center electron temperature is shown in Figure 6. The DD neutron yield for each shot is listed parenthetically in the legend.
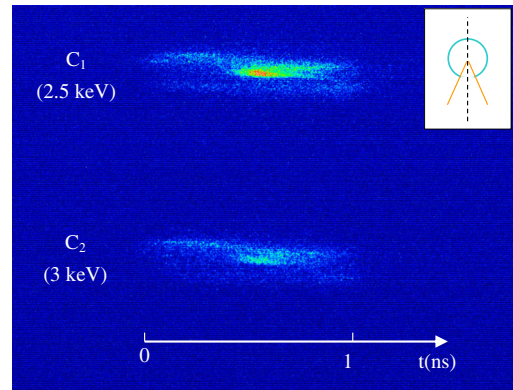

Fig. 5. Core radiation images of imploded cone-shell target recorded by dual-spectral KB streak camera. The inset at the top-right corner illustrates the orientation of the cone-shell target, and the dashed line shows the relative position of the streak camera entrance slit.
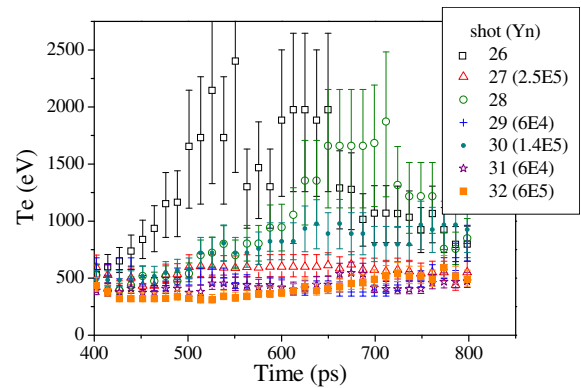

Fig. 6. Evolution of cone-shell target core electron temperature. Target surface starts radiation at time zero. The legend also shows the neutron yield corresponding to shots.

Figure 6 shows that the shock wave reaches the shell center at 400 ps. The temperature at this time is 500 ± 100 eV, which is consistent from shot to shot. This consistency leads us to believe that the temperature derived from multispectral imaging is credible.

There appears to be no clear relationship between temperature from multispectral imaging and neutron yield, which indicates a non-uniform temperature distribution in the hot spot. Neutron reaction rates are very sensitive to temperature [23], so a local small-scale high-temperature will cause a significant increase in neutron yield. In the case of non-uniform temperature distribution, neutron yield is not a good indicator of the hot-core internal energy.

5 Conclusions

The temperature distribution evolution of the hot spot is a key physical quantity for fast ignition inertial confinement fusion experiments. The temperature measurement method using multispectral diagnosis of continuum radiation is suitable for a sub-keV to several keV hot spot with

small external fuel areal density (relates to the measured photon energies, lower than 100 mg/cm^2 for CD shell and measured photon energy of 2.5 keV). Multispectral imaging using a multichannel KB microscope has the advantages of high photon collection efficiency, appropriate and controllable spectral resolution, and easy coupling with temporal resolution recording equipment such as streak cameras or framing cameras. Experimental results prove the feasibility of multispectral X-ray imaging method of temperature measurement under these conditions. By further optimizing the imaging system design, this method is expected to provide an effective hot-spot temperature diagnosis method for fast ignition integrated experiments.

References

1. M. Tabak et al., Phys. Plasmas **1**, 1626 (1994)
2. R.L. McCrory et al., Eur. Phys. J. D **44**, 233 (2007)
3. X.T. He, W.Y. Zhang, Eur. Phys. J. D **44**, 227 (2007)
4. R. Kodama et al., Nature **412**, 798 (2001)
5. R. Kodama et al., Nature **418**, 933 (2002)
6. M. Koga et al., Nucl. Instrum. Methods Phys. Res. A **653**, 84 (2011)
7. W. Theobald et al., Phys. Plasmas **18**, 056305 (2011)
8. V.Y. Glebov et al., Rev. Sci. Instrum. **75**, 3559 (2004)
9. S. Fujioka et al., Rev. Sci. Instrum. **81**, 10E529 (2010)
10. J.R. Rygg et al., Science **319**, 1223 (2008)
11. M.D. Cable et al., Rev. Sci. Instrum. **63**, 4823 (1992)
12. J.A. Koch et al., J. Quant. Spectrosc. Radiat. **88**, 433 (2004)
13. R. Tommasini et al., Rev. Sci. Instrum. **77**, 10E303 (2006)
14. F.J. Marshall et al., Rev. Sci. Instrum. **68**, 735 (1997)
15. F.J. Marshall, Rev. Sci. Instrum. **83**, 10E518 (2012)
16. B.Z. Mu et al., High Power Laser and Particle Beams **25**, 903 (2013)
17. J.Y. Zhong et al., Rev. Sci. Instrum. **79**, 10E907 (2008)
18. F. Bridou et al., Rev. Sci. Instrum. **73**, 3789 (2002)
19. I. Uschmann et al., Appl. Opt. **39**, 5865 (2000)
20. K. Fujita et al., Rev. Sci. Instrum. **72**, 744 (2001)
21. G.B. Rybicki et al., *Radiative processes in astrophysics* (Wiley, New York, 1979)
22. I.H. Hutchinson, *Principles of plasma diagnostics*, 2nd edn. (Cambridge University Press, New York, 2002)
23. L.M. Hively, Nucl. Fusion **17**, 873 (1977)